Delft University of Technology

Aerodynamic Design of a Flying V Aircraft in Transonic Conditions

Laar, Y.A.; Atherstone, D.M.; Benad, J.; Vos, Roelof

DOI
10.2514/6.2024-2669

Publication date
2024

Document Version
Final published version

Published in
Proceedings of the AIAA SCITECH 2024 Forum

Citation (APA)
Laar, Y. A., Atherstone, D. M., Benad, J., & Vos, R. (2024). Aerodynamic Design of a Flying V Aircraft in Transonic Conditions. In *Proceedings of the AIAA SCITECH 2024 Forum* Article AIAA 2024-2669 American Institute of Aeronautics and Astronautics Inc. (AIAA). https://doi.org/10.2514/6.2024-2669

Important note
To cite this publication, please use the final published version (if applicable).
Please check the document version above.

Copyright
Other than for strictly personal use, it is not permitted to download, forward or distribute the text or part of it, without the consent of the author(s) and/or copyright holder(s), unless the work is under an open content license such as Creative Commons.

Takedown policy
Please contact us and provide details if you believe this document breaches copyrights.
We will remove access to the work immediately and investigate your claim.

This work is downloaded from Delft University of Technology.
For technical reasons the number of authors shown on this cover page is limited to a maximum of 10.

AIAA SciTech Forum
8-12 January 2024, Orlando, FL
AIAA SCITECH 2024 Forum

10.2514/6.2024-2669

Aerodynamic Design of a Flying V Aircraft in Transonic Conditions

Yuri Laar*, Daniel Atherstone †, Justus Benad ‡ and Roelof Vos §
Delft University of Technology, Kluyverweg 1, 2629HS Delft, the Netherlands

The Flying V is a long-range, flying-wing aircraft where payload and fuel both reside in a V-shaped, crescent wing with large winglets that double as vertical tail planes. The objective of this study is to maximize the lift-to-drag (L/D) ratio of the Flying V in cruise conditions, i.e. $C_L = 0.26$, $M = 0.85$ and to investigate its off-design performance in high-subsonic conditions. This is done by manually modifying the design parameters that describe the outer mold line of the Flying V and assessing the aerodynamic performance by means of computational fluid dynamics. A 15-million cell, third-order MUSCL, Reynolds-Averaged Navier Stokes solver with the Menter SST turbulence model is used to estimate the aerodynamic coefficients. This numerical model is validated using the experimental data of the ONERA M6 wing. A new, CATIA-based, parametrization of the Flying V is the starting point of the design. Three manual design phases improve the aerodynamic performance while satisfying all constraints. Design modifications include an increase in camber and aft-loading of the wing around 40% of the semispan and improved airfoil sections on the outboard wing generating the required lift coefficient towards an elliptical lift distribution. The twist distribution at the wing-winglet junction is optimized to reduce wave drag. This has resulted in an improvement of L/D from 20.3 from previous studies to 24.2 for the final version, while reducing the cruise angle of attack from 5.2 to 3.6 degrees. The drag divergence Mach number is estimated at 0.925.

Downloaded by Technische Universiteit Delft on January 5, 2024 | http://arc.aiaa.org | DOI: 10.2514/6.2024-2669

Nomenclature

Latin Symbols

b	Span (m)
C	Chord Length (m)
C_D	Drag Coefficient (-)
C_L	Lift Coefficient (-)
C_M	Moment Coefficient (-)
C_P	Pressure Coefficient (-)
H	Cabin Height Parameter (m)
k	Turbulence Kinetic Energy (J)
L	Planform Length Parameter (m)
M	Mach number (-)
P	Pressure (Pa)
T	Temperature (K)
$\tilde{u}_i$	Favre-Averaged Velocity (m/s)
u''_j	Velocity Fluctuation (m/s)
w	Cabin Width Parameter (m)

Greek Symbols

ϵ	Dissipation Rate (m^2/s^3)
θ	Skewness Angle (deg)
Λ	Sweep Angle (deg)
μ	Dynamic viscosity (Pas)
ρ	Density (kg/m^3)
ω	Specific Dissipation Rate (1/s)

Sub- and Superscripts

cop	Center of Pressure Position
crit	Critical Pressure Coefficient
in	Inboard wing
L	Leading Edge
np	Neutral Point Position
out/O	outboard wing
R	Wing Root
T	Wing Tip
TE	Trailing edge

Acronyms

3DX	3DEXPERIENCE
GCI	Grid Convergence Index
L/D	Lift-to-Drag Ratio
MAC	Mean Aerodynamic Chord
MUSCL	Monotonic Upstream-centered Scheme

*MSc Student, Faculty of Aerospace Engineering
†Education & Research Assistant, Faculty of Aerospace Engineering
‡Postdoctoral Researcher, Faculty of Aerospace Engineering
§Associate Professor, Faculty of Aerospace Engineering, r.vos@tudelft.nl, Associate Fellow AIAA

Copyright © 2024 by Yuri Laar, Daniel Atherstone, Justus Benad, Roelof Vos. Published by the American Institute of Aeronautics and Astronautics, Inc., with permission.

ORP	Oval Retention Parameter	SST	Shear Stress Transport
S-A	Spalart-Allmaras		

I. Introduction

After two years of COVID-19 travel restrictions, the aviation industry has recently been recovering from the reduced number of passenger traffic. As of September 2023, the number of flights is at 90% of pre-COVID-19 numbers [1]. Looking forward, Airbus predicts a yearly growth rate of 3.9%, leading to double the passenger traffic in 2040, with respect to pre-COVID-19 world annual traffic [2]. While this growth might be beneficial from an economic standpoint, an increase in flights leads to a potential increase in emissions. With the European goal of a reduction of carbon dioxide emissions of 55% in 2030 and climate neutrality in 2050 [3], this growth leads to significant challenges.

Part of the solution lies in a more efficient aircraft shape, increasing the lift-to-drag ratio (L/D). Current aircraft, separating lifting surface (the wing) and payload structure (the fuselage), are seeing diminishing improvements in efficiency over time [4]. Ever since the start of fixed-wing aviation, engineers and designers have tried to move away from this tube-and-wing configuration, towards less conventional configurations. Whether a larger efficiency, more range, more carrying capacity or stealth is the objective, the flying wing and blended wing body (BWB) have shown promising characteristics throughout history. The first functional practical flying-wing concepts arose in Europe around 1910. Inspired by the glider experiments of Otto Lilienthal, one of the first working prototypes was created by J. W. Dunne, with the Dunne D.8 [5]. The Second World War brought new attention to flying wings for a military purpose with the benefit of an extended range and flight time, combined with a practical shape for carrying ordinance. The Germans designed the Horten Ho 229 and the Americans designed what would ultimately become the Northrop YB-35.

A different approach is to retain a fuselage-like section, in the form of a blended wing body. An example of this is the Airbus ZEROe BWB.* The transonic airliner blended wing body consists of an inboard wing/passenger section with a high thickness-to-chord ratio and a more traditional outboard wing incorporating supercritical airfoils, as described by Liebeck [6]. While multiple studies show the promising efficiency gains of such a configuration [7–10], the aft-positions of the neutral point and center of pressure lead to a small moment arm of the control surfaces. This necessitates a large control surface area and results in potential trim drag penalties [7].

Fig. 1 Artist impression of the Flying V

Building on the last hundred years of unconventional planform design, Benad [11, 12] envisioned a new flying wing concept at the Airbus Future Projects office in Hamburg: the Flying V. As the passengers sit in the V-shaped wing, the lift-producing area is increased with respect to a traditional aircraft, while the wetted area is reduced. The Flying V promises the efficiency benefits of blended wing bodies, while adhering to logistical constraints similar to the A350 and avoiding the need for an extraordinarily large control surface area [13].

The first aerodynamic design was based around the Airbus ODILIA tool, a 3D vortex lattice method. The tool allowed for the optimization of the aircraft wing twist, striving for an elliptic lift distribution. After Benad's original study, the Flying V was further aerodynamically optimized by Faggiano in 2016 [14]. Faggiano implemented Euler solver SU2, together with panel code AVL, into the knowledge-based engineering ParaPy environment †. The overall result of the design study was an increase in lift-to-drag ratio from 22.8 to 23.7. Furthermore, the work done increased

*See www.airbus.com, accessed 28 November 2023.

†See parapy.nl, accessed 28 November 2023.

Downloaded by Technische Universiteit Delft on January 5, 2024 | http://arc.aiaa.org | DOI: 10.2514/6.2024-2669

the fidelity of the aerodynamic performance estimations. Hillen [15] redefined the parametrization, taking into account cabin flexibility and manufacturability. Expanding on the work of Hillen, Oosterom [16] investigated the conceptual creation of a Flying V family, altering the parametrization again. Oosterom demonstrated that for a 20% reduction in fuel consumption with respect to the Airbus A350, the Flying V needed to have lift-to-drag ratio of at least 20.6. While Hillen and Oosterom used VLM methods for the aerodynamic optimization, Van Luijk [17] performed an optimization of the outer wing, using an Euler-based simulation in combination with a Free-Form Deformation algorithm. The parametric geometry model in ParaPy showed shortcomings in the shapes that could be generated leading to sharp transitions between sections. Therefore, the highest L/D obtained for the Flying V without engines was only 20.3. To overcome these shortcomings, a new CATIA-based parametrization was devised by Benad. This parametrization is the starting point of this study.

The goal of this study is to maximize the lift-to-drag ratio of the Flying V in cruise conditions by modifying the design parameters that describe its outer mold line. A manual approach to optimization is taken, where based on physical insights the design parameters are altered. The design should adhere to practical constraints regarding structural design, internal volume, and control surface integration. The aerodynamic assessment is done by means of computational fluid dynamics (CFD) where the Reynolds-Averaged Navier Stokes (RANS) equations are solved numerically on a structured mesh.

The paper is structured as follows. Section II describes the parametrization, simulation set-up, and optimization workflow. Section III validates the workflow described in Section II. With the methodology established and validated, Section IV presents the results and findings of the study. Conclusions are drawn in section V.

Downloaded by Technische Universiteit Delft on January 5, 2024 | http://arc.aiaa.org | DOI: 10.2514/6.2024-2669

II. Methodology

This section presents the parameterization of the Flying V, the simulation set-up, and the optimization procedure used in this study. The Flying V is parametrized in 3DEXPERIENCE CATIA (3DX), ensuring a smooth transition between the various sections of the wing. The aerodynamic simulation is run in ANSYS Fluent using a 3rd-order MUSCL Reynolds Averaged Navier-Stokes simulation. The model is manually optimized to reduce simulation costs and more easily take into account the multidisciplinary aspects of the project. While Oosterom and Vos designed the Flying V as a three-member family, in this study only the largest variant is used for optimization [16]. This is the Flying V-1000

A. Parametrization

The layout of the Flying V-1000 is visualised in Figure 2a. The cabin has a 2-class configuration, seating 378 passengers. The business class is located near the nose of the aircraft with economy in the two wing sections. Cargo is stored further back, as the thickness-to-chord ratio in this region starts to decrease. Fuel is stored in the trailing edge as well as in the outboard wing. Wing trunks of constant cross section are part of the inner wing. These trunks with designations "-900" and "-1000" can be omitted to create two smaller family members of the Flying V. The Flying V wing planform can be characterized as a crescent wing, with an inboard wing having a higher sweep angle than the outboard wing.

The parameterization of the Flying V planform is displayed in Figure 2b. This parameterization follows the parameterization as laid out by Hillen[15] but is now implemented in 3DX and further expanded. The inboard wing consists of an oval cross-section as proposed by Vos et al. [19] while the outboard wing has a more traditional airfoil profile. A distinct feature of the new model is the oval retention parameter (ORP) [20]. The ORP determines where the oval cross-section ends and the interpolation to the outboard wing profiles starts. This parameter facilitates a trade-off choice between aerodynamic performance and cabin space. In the creation of the new parametric model, the parameters were set by Benad as an engineering judgment based on the knowledge of previous studies. This initial version is here referred to as the "baseline design."

The wing chord (C_R) of the untapered part of the inboard wing is defined orthogonally to the leading edge of the wing. At station 3 the wing chord (C_3) is defined perpendicular to the leading edge of the inboard wing. The cabin width, w_1 and w_3, are important in shaping the sections, as these parameters determine where the cabin section transitions to the trailing edge section, as seen in Figure 2b. Sweep angles Λ_{in} and Λ_{out} determine the sweep of the leading edge of the inboard wing and outboard wing, respectively. Then, the outboard wing is defined by two sections that each are oriented parallel to the direction of flight: $C_{O,R}$ and $C_{O,T}$. Finally, the winglet is defined by positioning two airfoils in the direction of flight and applying a smooth transition between the outer wing and the winglet.

Figure 3 shows a cross-section of the inboard wing with constant cross section, orthogonal to the leading edge. The parameter H_w is introduced, which fixes the height of the maximum width of the fuselage, w_H. Parameters H_1 and H_3 are important in defining the camber of the profile as more or less area can be added below or above the chord line. The

Downloaded by Technische Universiteit Delft on January 5, 2024 | http://arc.aiaa.org | DOI: 10.2514/6.2024-2669

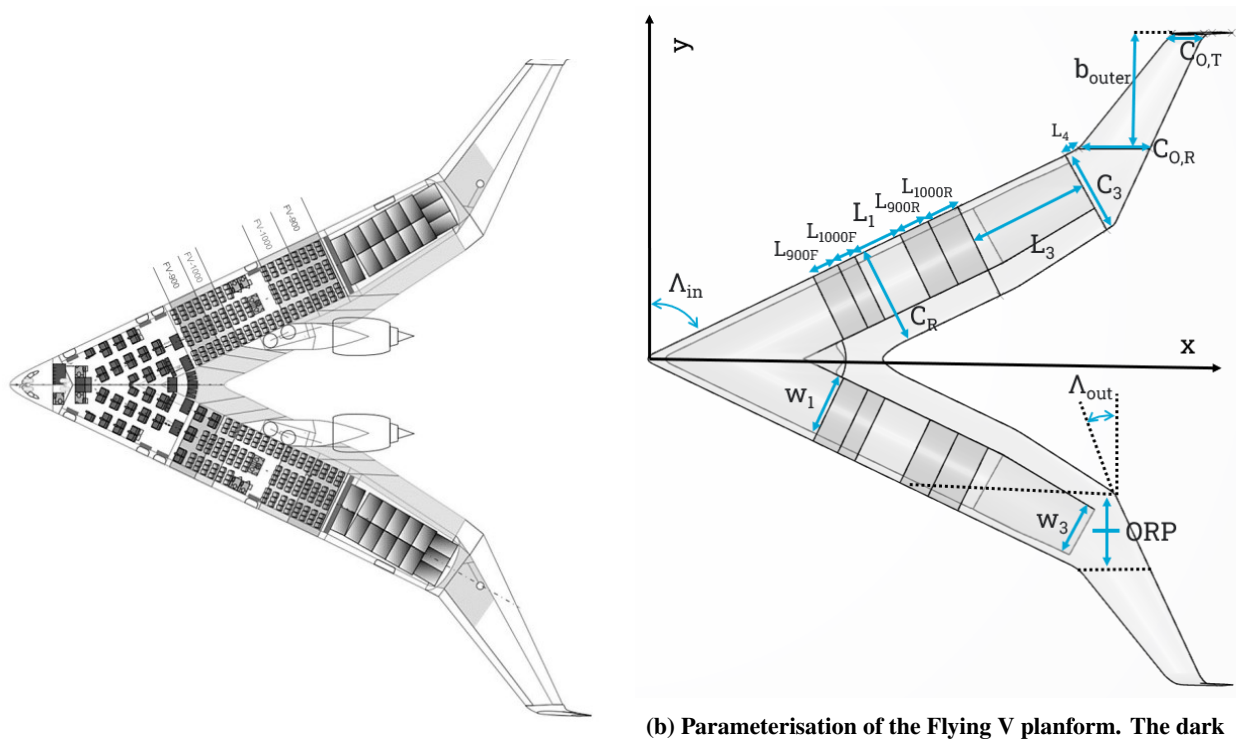

(a) Layout of the Flying V 1000 in a 2-class configuration, seating 378 passengers [18]

(b) Parameterisation of the Flying V planform. The dark grey sections are part of the family design and can be omitted in different versions.

Fig. 2 Parametrization and layout of the Flying V planform

trailing edge height, z_{TE} and the trailing edge angles, $\angle open$ and $\angle inc.$, also influence camber and aft-loading.

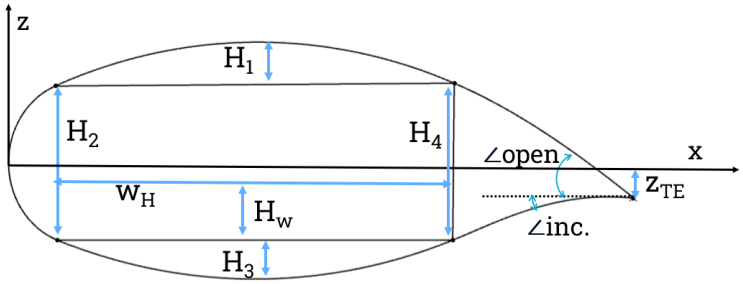

Fig. 3 Cross-sectional parametrization of the Flying V

The complete geometry of the Flying V is described in 3DX by 97 parameters. Except for the trailing edge, the transitions between the various wing components are made C2 continuous (i.e. continuous curvature) by applying local blending over the seams between the various components. Neither the engine nor any other aerodynamic body is part of the outer mold line in this study. We concentrate solely on the wing.

B. Numerical Setup

The research uses ANSYS Fluent for the simulations and ANSYS ICEM for the meshing. ANSYS Fluent is a well-validated tool [21]. ANSYS ICEM is a tool especially suitable for structured meshes, which is the focus of this research. As the simulation is too large to run locally, the Aerospace faculty's high-performing cluster (HPC) is used for the simulations. The transonic conditions of the simulation require a coupled density-based approach, where time stepping is used to converge the simulation [22]. The Favre and Reynolds averaged Navier-Stokes equations [21] are

solved as a trade-off between accuracy and computational cost.

The starting point of the simulation is the computational grid, which needs to meet specific criteria detailed later in the paper. A structured mesh is the preferred option for this simulation, as the geometry is relatively simple and significant gains can be achieved with structured meshes compared to unstructured meshes [22]. An O-mesh is the preferred option around the airfoil, as a blunt trailing edge is present in the Flying V parametrization. No singular point arises, which would occur with a sharp trailing edge combined with a C-mesh. The O-mesh will curve around the Flying V winglet (Figure 4), so special care is taken such that the curving of the mesh does not lead to excessively skewed elements.

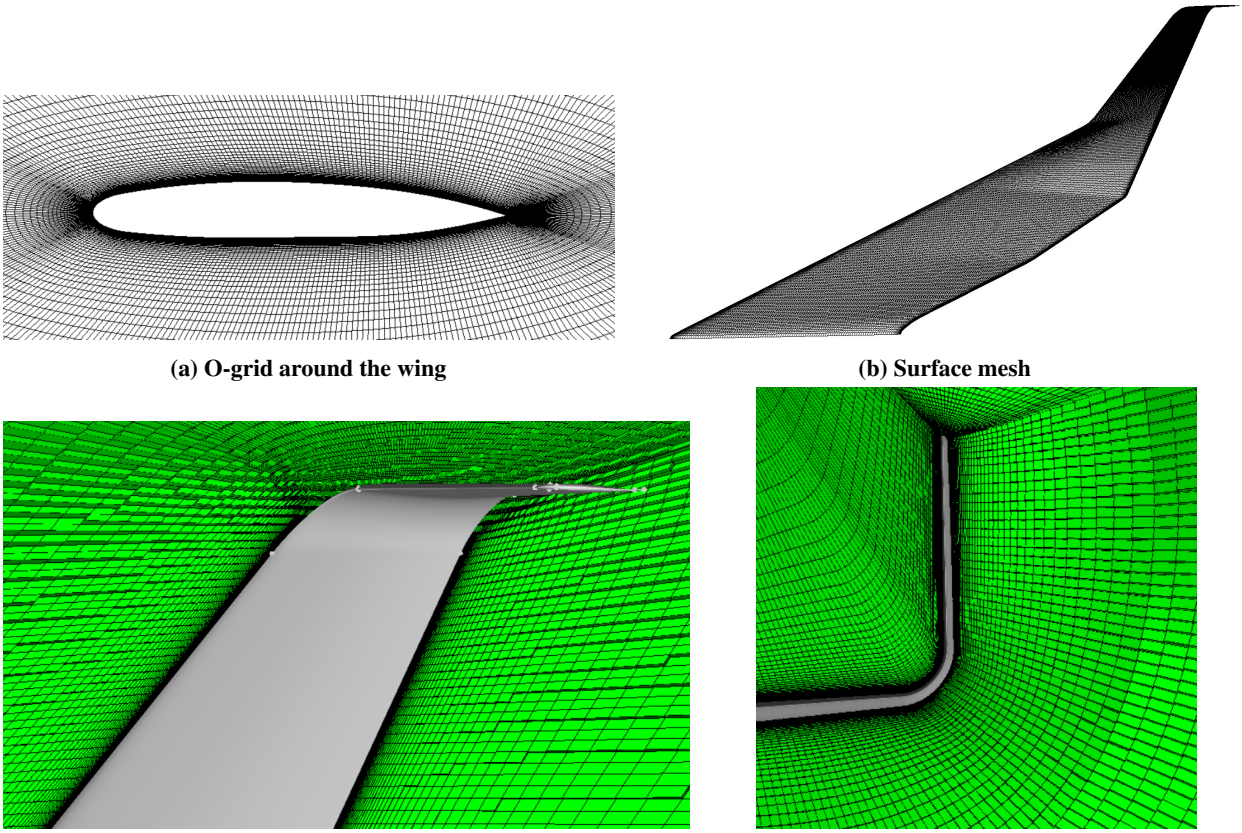

(a) O-grid around the wing

(b) Surface mesh

(c) Outboard wing, top view

(d) Outboard wing, front view

Fig. 4 Mesh visualisation at 15 million domain nodes

The computational domain is visualised in Figure 5. The domain is approximately 50 times the length of the root chord (parallel to the flow) of the Flying V to reduce artificial boundary errors, as recommended by Gotten [23]. A far-field pressure boundary condition is applied at the spherical boundaries, which approximates flow perturbations using the Euler equation Riemann invariants [21]. No-slip boundary conditions are applied on the smooth half-wing. A symmetry condition is applied at the half-plane.

The mesh is subjected to the following criteria: The determinant is the most important factor in a structured mesh [24]. It is a measure of the smallest divided by the largest determinant in the Jacobian matrix. A determinant of 1 dictates a totally regular mesh element, a negative determinant implies an inverted edge. The minimum value is kept above 0.3, following ANSYS guidelines[24].

The streamline spacing of the grid follows the recommendation of Rumsey, in a NASA assessment of current CFD capabilities: no more than 0.1% of the chord near the leading edge and 0.2% of the chord near the trailing edge [25]. In the wake, the grid is aligned with the trailing edge bisection angle to align the grid with the flow direction [25]. Following Goetten et al. [23], 135 cells in the chord direction on the lifting surface are used. The **skewness**, expressed by angle θ, is important to avoid numerical instabilities. Skewnesses of $\theta < 30°$ and $\theta > 150°$ are set as limits. Close to the wall θ is set close to 90 degrees [26]. The flowfield is initialized using a hybrid initialization method, which couples a

Downloaded by Technische Universiteit Delft on January 5, 2024 | http://arc.aiaa.org | DOI: 10.2514/6.2024-2669

Downloaded by Technische Universiteit Delft on January 5, 2024 | http://arc.aiaa.org | DOI: 10.2514/6.2024-2669

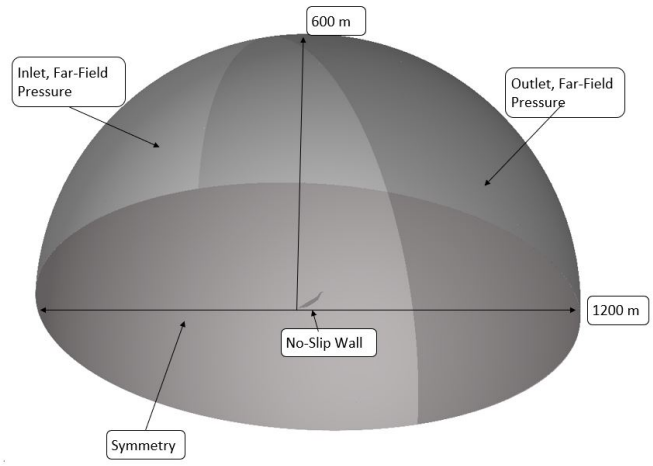

Fig. 5 Grid computational domain with dimensions and boundary conditions

potential flow simulation with the boundary layer equations [21]. The simulation is started in first-order, as higher-order simulations require a good initial estimate, due to the dependence on higher-order terms $\left(\frac{\Delta^2\phi}{\Delta x^2}, \frac{\Delta^2\phi}{\Delta y^2} >> u\frac{\Delta\phi}{\Delta x}, v\frac{\Delta\phi}{\Delta y}\right)$ [26]. Next, the simulation is converged using the intended higher order scheme (3rd order MUSCL[21]), while progressively increasing the CFL number to speed up convergence. An implicit scheme is used to guarantee stability and reduce computational costs. The flux over cell boundaries is computed using the Roe Flux-Difference Splitting Scheme [27]. Gradients are computed using a least squares cell-based approach [21]. The low Reynolds Menter SST turbulence model is used for its good inner layer resolving qualities compared to the $k-\epsilon$ model [28]. An algebraic multigrid solver is used, in which corrections on coarse levels are performed using the finer grid levels to accelerate convergence speed, based on the work of [29]. This creates a close to linear relation between grid size and convergence speed [21].

C. Optimization Workflow

In this study a manual iteration approach is performed to optimize the aerodynamic efficiency (L/D) of the Flying V in the design condition. Physical insights by the authors based on the results of the aerodynamic simulations dictate the direction of optimization. This approach offers an additional benefit by enabling a more direct consideration of trade-offs between aerodynamic improvements and potential volume and structural drawbacks.

The simulation workflow is visualized in Figure 6. The first step is to analyze the results and implement changes in the CAD model. As the design of the Flying V is highly coupled, it is checked if the proposed aerodynamic changes leave sufficient volume/dimensions in the wing section and if the structural changes are acceptable (stage 3). The inboard wing is constrained by its dimensions and volume, which is required to carry passengers/cargo. The outboard wing is characterized by thickness-to-chord ratio constraints of 10% and 8 % at the respective root and tip sections. The output of stage 2 serves as the input for the meshing and solver input (stage 4). The blocking of the structured mesh is reassigned, such that the iterations have similar meshes. Again the mesh criteria are checked and the node distribution is slightly altered to take into account the changed geometry. The resulting Fluent case serves as input for the aerodynamic solver (stage 5), run on the HPC. This step normally requires 2 iterations to get the right lift coefficient. The lift slope changes slightly between the iterations, such that usually the estimated lift coefficient of the second iteration agrees with the estimated required angle of attack. Stage 6 consists of the post-processing of the simulation data. ANSYS CFD-POST is used to generate visual data and to export data of over 14 individual wing sections, spaced 2.5 meter apart. A Python script is used to translate this data into pressure, lift and drag distributions. The lift and drag distributions are calculated based on pressure and skin friction coefficient of section elements. Finally, the location of the neutral point and center of pressure are evaluated.

In a trimmed state, the center-of-gravity should be ahead of the neutral point (equal to the aerodynamic center in this

Downloaded by Technische Universiteit Delft on January 5, 2024 | http://arc.aiaa.org | DOI: 10.2514/6.2024-2669

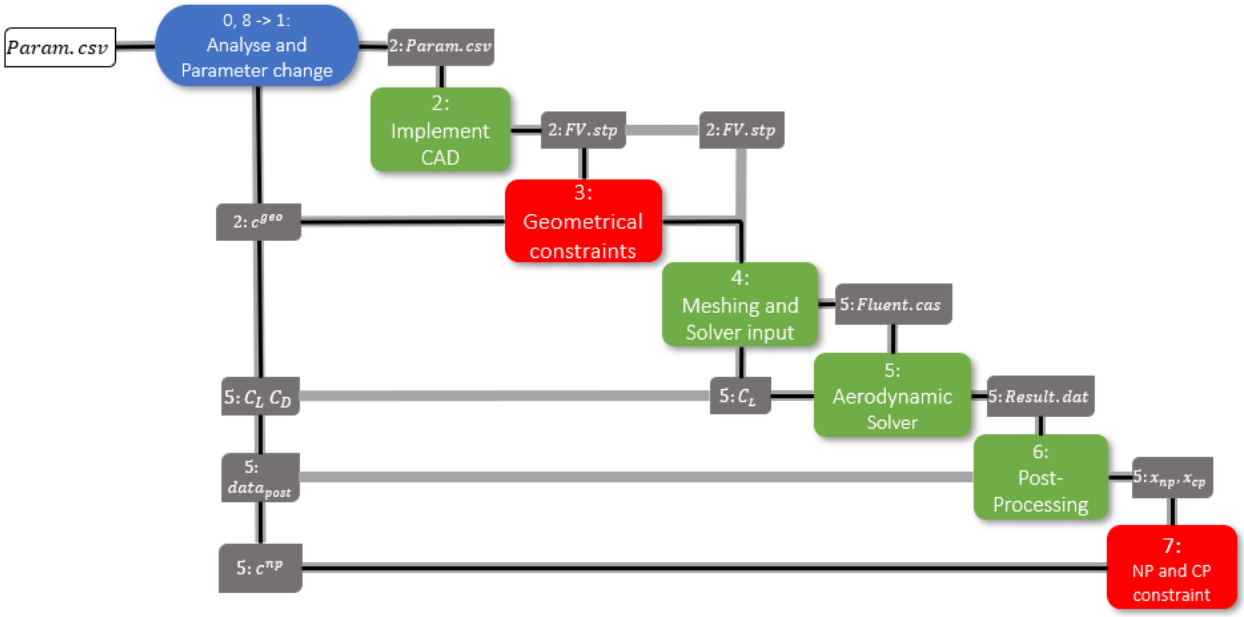

Fig. 6 Optimization workflow followed in this study.

case) to ensure static longitudinal stability. This stability constraint is formulated as follows:

$$(x_{np} - x_{cp})/MAC > 0.02 \tag{1}$$

While the center of pressure is computed in the simulation, the neutral point is estimated using the following equation:

$$\frac{x_{np} - x_{ref}}{\bar{c}} = \frac{x_{ref}}{\bar{c}} - \left(\frac{\partial C_{M_{ref}}}{\partial C_L}\right) \tag{2}$$

Three angle-of-attack computations are used for the estimation of the neutral point and linear regression is used to determine the slope of the moment curve at the design lift coefficient.

III. Verification and Validation

Verification and validation are an integral part of any simulation-based optimization process to guarantee the reliability of the simulation. Tu et al. [26] describe verification as the degree to which the model does what the user developed it to do and validation of the degree to which the model agrees with reality. We first discuss the verification of the method and subsequently the validation of the solver.

A. Verification

A grid convergence study aims to determine the ordered discretization error of a set of simulations. The temporal and spatial discretization errors should converge to zero asymptotically, as the grid and timestep are refined. The goal of the study is to estimate the perceived order of the method and determine a suitable number of grid cells at which the simulation can reliably be run, while minimizing the simulation costs. The NPARC verification procedure is followed [30], of which the methods are largely based on the book by Roach [31]. Richardson extrapolation [31] can be used to estimate the order of the method. This requires three solutions in the asymptotic range of convergence on three different grid spacings. With the order of convergence of the simulation known, the required number of grid cells can be estimated based on a required grid convergence index (GCI), which gives an indication of the magnitude of the normalized discretization error.

In this verification study, the baseline Flying V geometry is utilized to investigate the effect that the number of nodes has on the value of the lift coefficient. The conditions that are evaluated are as follows: $M = 0.85$, $C_L = 0.26$,

and Re = 88.3 million. The first three runs in the asymptotic region are the runs of 1M, 2.5M and 5M nodes. Using Richardson extrapolation, the perceived order of spatial convergence is estimated to be 3.5. This is reasonably close to the 3rd-order MUSCL method that is used as the spatial discretization scheme in the simulation. As refining a grid consistently in a structured mesh is relatively hard, as nodes are specified by the user in each block or subsection of the simulation domain, some inconsistency in the perceived order of convergence is expected.

Figure 7a shows the full spatial convergence study. The 5 million nodes mesh gives a GCI of 0.8%. Based on the examples and guidelines given in [30] and [31], together with the focus on reliability in the research project, a GCI of 0.01% is deemed acceptable, corresponding to a mesh density of 15 million nodes. The computed GCI from the simulated case is 0.0092%, thus acceptable. The reason for this relatively low GCI lies in the fact that this research focuses on manual optimization steps, instead of having an optimizer exploring the design space. This leads to a significantly reduced number of total simulations performed and allows for stricter requirements on the accuracy of the simulation compared to previous studies [17], especially in this complicated fluid domain.

Downloaded by Technische Universiteit Delft on January 5, 2024 | http://arc.aiaa.org | DOI: 10.2514/6.2024-2669

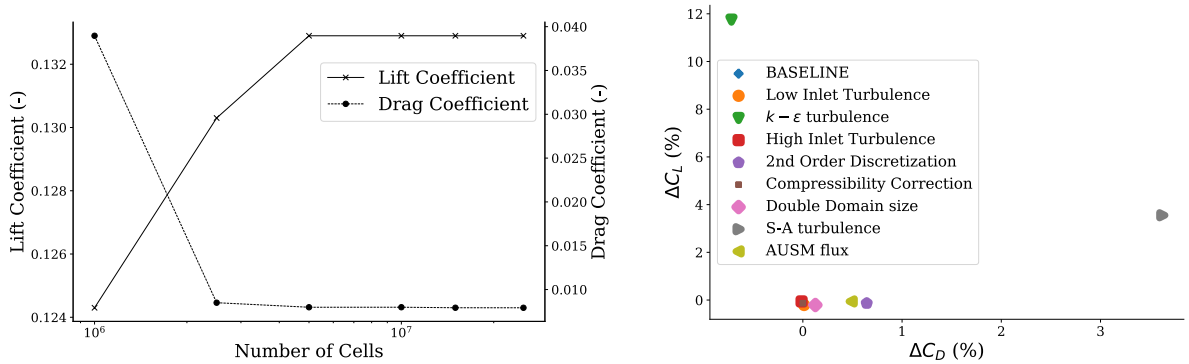

(a) Flying V baseline wing mesh convergence study

(b) Flying V sensitivity study

Fig. 7 Flying V Mesh convergence and sensitivity studies

As the simulation depends on several assumptions and model choices, it is important to quantify the effect these choices have on the simulation results. The baseline simulation uses the Menter SST turbulence model, combined with a third-order MUSCL spatial discretization scheme with 1 % inlet turbulence. Therefore, various combinations of model choices are explored. Table 1 presents an overview of the modelling variations that are evaluated. Figure 7b shows the percentage difference in lift coefficient between various modelling variations. It can be seen that a relatively large dependency exists on the turbulence model that is chosen. The $k-\epsilon$ results can be questioned, as the high Reynolds-number model, in combination with a wall model might not perform well near the wall in complicated flows [32]. The 3-4% difference in results of the Spalart-Allmaras model should be considered as an uncertainty margin.

Table 1 Uncertainty parameters

Index name	Modeling variation	Explanation
$k-\epsilon$ turbulence	Turbulence model	Realizible $k-\epsilon$ turbulence model, including a wall model
S-A turbulence	Turbulence model	Spalart-Allmaras vorticity based turbulence model
Compressibility Correction	Turbulence model	Menter SST turbulence model with a compressibility correction
Low Inlet Turbulence	Turbulence model	0.1% turbulence inflow conditions
High Inlet Turbulence	Turbulence model	10% turbulence inflow conditions
2nd Order Discretization	Discretization scheme	Second order upwind scheme
AUSM flux	Discretization scheme	AUSM flux type
Double Domain size	Domain	Radius of the domain doubled for artificial boundary influence

Downloaded by Technische Universiteit Delft on January 5, 2024 | http://arc.aiaa.org | DOI: 10.2514/6.2024-2669

B. Grid Quality

Simultaneously to the grid convergence study, the quality of the generated meshes has to be ensured. Especially while refining a mesh, erroneous elements can cause instability, non-convergence and a higher cost of simulation. An overall poor-quality mesh can lead to unreliable results. A certain number of objective grid quality parameters can be set up to evaluate the quality of the mesh. The mesh quality criteria in a hexahedral structured mesh differ from the criteria of a tetrahedral unstructured mesh due to the nature of the orientation of the cells [33]. Three important indications of a good structured mesh are the determinant [24] indicating the quality of a cell, the minimal or skew angle [23], indicating the orientation of the cell and the y^+ value, important for the turbulence model[28].

Another important aspect of the quality of a structured mesh is the determinant. It gives an indication of the quality of the cell, whether the edges of the cell are orientated properly or not. A minimum value of 0.3 is recommended [34]. A determinant close to zero indicates a block close to inversion. Figure 9 shows the determinant distribution of the Flying V mesh. Overall, the determinant is close to 1, indicating that most blocks resemble a hyperrectangle. The largest deterioration of the mesh occurs near the tip of the winglet. At this section the mesh has to both, curve back towards the z-x plane, orthogonal to the wing root section, and the blocks start to expand towards the outer boundary. This can also be seen in figure 4d. Especially the blocks near the boundary are the most critical here. Their determinant value is still deemed sufficient.

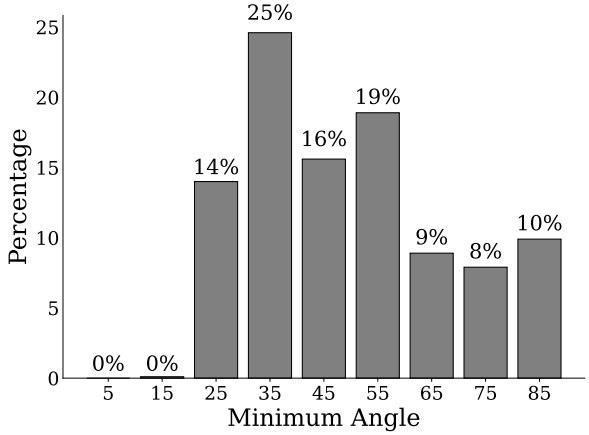

Fig. 8 Flying V mesh min angle

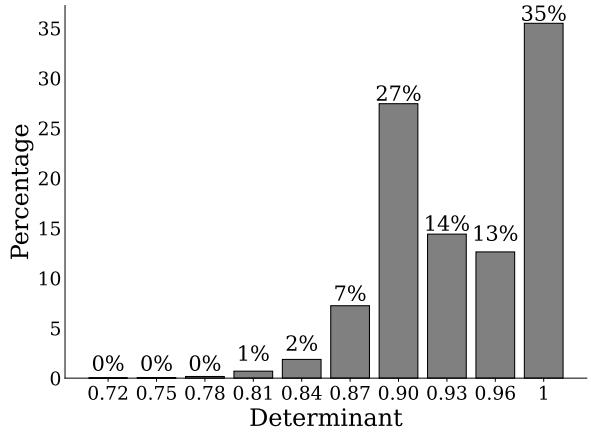

Fig. 9 Flying V mesh determinant distribution

The third quality of a structured mesh is the minimum angle. The term 'minimum angle' concerns the smallest angle formed by any of the faces of a hexagonal cell [24]. The minimum angle that ANSYS Fluent can handle is 8 degrees [24]. However, a value of 30 degrees is desirable from a convergence perspective. Figure 8 shows the minimum angle distribution of the Flying V mesh. The relatively high deviation from the ideal 90-degree hexagonal element can be explained by the spherical shape of the domain, the high sweep of the wing and the curvature of the mesh around the winglet. The choice for a structured mesh, in combination with a spherical domain, leads to a relatively poorer skewness distribution than an unstructured mesh in a conical domain would. The alignment of the mesh with the flow, the structured nature and the smooth transition from boundary layer to outer mesh do however compensate for this behaviour and, as shown in the Validation section, lead to satisfactory results.

Finally, we evaluate how well the boundary layer is modelled. Figure 10 shows the y^+ distribution on the wing. This value should be below one to sufficiently capture the viscous sublayer near the wall [28]. The wall-normal distance of the first cell is set equally (at 0.008 mm) at every stage of the wing, so the difference in y^+ will be caused by changes in wall shear stress, thus velocity gradient, and density, thus velocity. Overall the y^+ value is well below one. The viscous sublayer should be well represented, combined with the growth rate of the first cell of 1.25. This is the maximum ratio advised for Navier-Stokes-based RANS codes by Spalart [35]. The highest y^+ value observed is 0.61 and occurs at the winglet junction, possibly due to the double shock occurring at this section. With changing flow conditions in different designs, the y^+ value should stay below one.

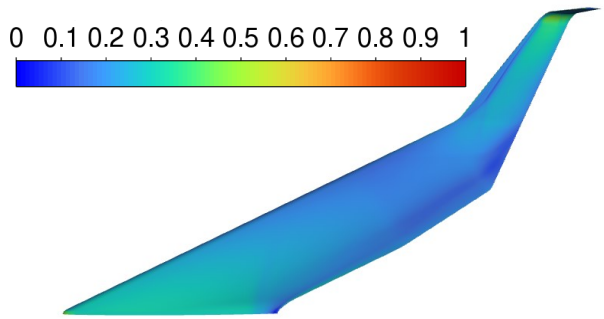

Fig. 10 y^+ **distribution on the upper surface of the Flying V half wing (Mach =0.85, Re = 88.3 million,** C_L **= 0.26)**

Downloaded by Technische Universiteit Delft on January 5, 2024 | http://arc.aiaa.org | DOI: 10.2514/6.2024-2669

C. Validation

The simulation set-up described in Section II is validated using the industry-standard experimental data of the ONERA M6 wing. The experimental data is obtained by Schmitt and Charpin at a Mach number of 0.8395, angle of attack of 3.06 degrees and Reynolds number of 11.72 million [36]. Even though the ONERA M6 wing differs from the Flying V, the same transonic behaviour, e.g. isentropic compression, shocks, boundary layer thickening, can be observed, covering the most important aspects of the simulation. The mesh is constructed according to the methodology described in Section II and consists of 4 million cells.

Figure 11 shows the comparison of pressure distribution of the validation simulation and experimental data by Schmitt and Charpin [36]. Three sections of the wing are shown at 65%, 90% and 95% of the semi-span. The numerical and experimental data correlate well at each of the span stations. The simulation captures the double shock at 65% semi-span as well as the single shock at 90% of the semi-span. Overall, the chordwise pressure distribution at each of these stations is captured almost perfectly by the simulation. The only deviation is the location of the first shock at $y/b = 0.80$, which is predicted to be a 5% more aft compared to the experimental results. The relatively fine, structured mesh used in the Validation study also captures certain shocks, like the shock at $y/b = 0.8$, which were not captured in previous validation studies performed by one of the authors [17, 37]. Also in comparison to the simulations of Ref. [38], the present simulation predicts the pressure distribution over the ONERA M6 wing very well.

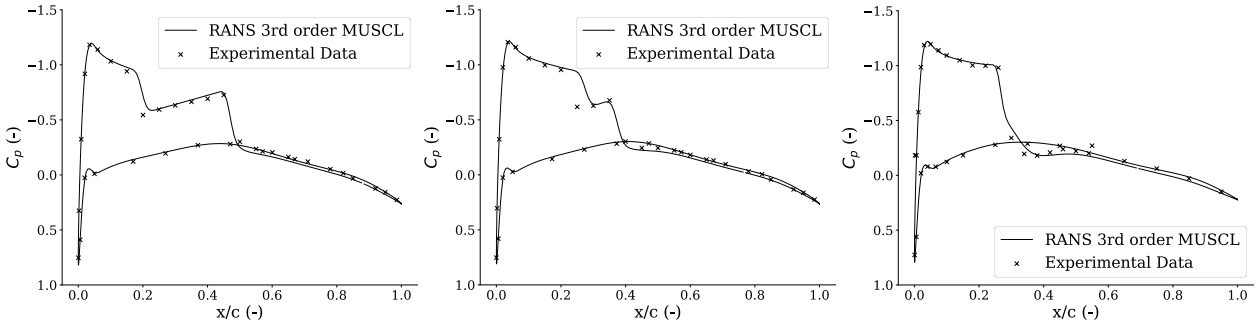

(a) y/b = 0.65 **(b) y/b = 0.80** **(c) y/b = 0.9**

Fig. 11 Pressure distribution validation on the ONERA M6 wing (Mach = 0.8395, $\alpha = 3.06$ **, Re = 11.72 million)**

Table 2 compares the aerodynamic coefficients of various numerical studies from the open literature to the results of this validation study. The drag coefficient is displayed in drag counts. The variation in lift and drag coefficients that are found in each of these studies is an indication for the inherent uncertainty margin in performing RANS simulations. For example, Ref. [39] predicts 168 drag counts, while Ref. [40] shows 189 counts for the simulation with the SST turbulence model. With $C_L = 0.268$ and $C_D = 171$ counts, the present simulation is within the range of the studies performed. The range of outcomes from various authors should be taken into account in the uncertainty margin of this study.

Table 2 Simulation set-up validation using numerical data of the ONERA M6 wing (Mach = 0.8395, α = 3.06°, Re = 11.72 million)

	Turbulence model	Spatial discretization	C_L (-)	C_D (drag counts)
Present study	SST	MUSCL + Roe FDS	0.268	171
Araya[40]	SA	Central dif. + JST	0.260	175
Araya [40]	$k-\omega$	Central dif. + JST	0.262	179
Araya [40]	SST	Central dif. + JST	0.253	189
Crovato et al.[38]	Baldwin-Lomax	Green gauss + JST	0.272	174
Le Moigne, Qin [39]	SA	MUSCL+Riemann	0.270	168
Nielsen, Anderson [41]	SA	2nd ord. upwing+ Riemann	0.253	181

IV. Results

With the set-up of the simulation validated, the Flying V in its current parametrization can be optimized. The optimization procedure is described in Section II. As this study focuses on cruise performance, the Flying V is optimized at cruise conditions. The top-level requirements of a Mach number of 0.85 and cruise altitude of 13 km lead to a design Reynolds number of 88.3 million. Based on the drag polar and top-level requirements, the geometry is optimized for a cruise lift coefficient of 0.26. The angle of attack is obtained through an iterative process.

Table 3 Flight conditions and reference values for the CFD simulations

Flight Conditions		Reference Values	
Cruise altitude	13.0 km	$\bar{c}$	19.0 m
Mach number	0.850	S_{ref}	880 m^2
Reynolds number	88.3×10^6	T	217 K
C_L	0.260	μ	1.43×10^{-5} Pa·s

The design activities are divided into three distinct phases. As the planform is based on numeral previous Flying V studies, the first phase focuses on the optimization of Flying V airfoil sections, leaving the planform unaltered. The objective is to find a balance between an elliptical lift distribution, wave drag, section performance and longitudinal static stability, which maximizes the lift-to-drag ratio. With the insights from Phase 1, Phase 2 aims to make relatively small planform changes to redistribute wing area. Local lift coefficients on sections that suffer high compressibility losses are reduced to relieve these sections. Conversely, other lightly loaded section get an increase in loading. These area distributions are intended to provide a more efficient lift distribution. Phase 3 focuses on the airfoils of the outboard wing. As open-source airfoils in the right flow regime are scarce, a two-dimensional optimization aims to create a new set of airfoils, suitable for the flow regime. The three-dimensional nature of the flow at the outboard wing changes the characteristics of the airfoil. Therefore multiple iterations are performed to obtain the optimal twist distribution of the new airfoils.

A. Aerodynamic Design Evolution

Throughout the three phases, a total of eight different designs are produced and evaluated in CFD. The complete set of geometries can be found in the thesis by Laar [42]. In Table 13 an overview of the design variations from one design to the next are presented. In addition, the second column lists the lift-to-drag ratio that was found for each design iteration. It can be seen that through evolutionary changes, the final lift-to-drag ratio is 24.2.

Figure 12 shows the evolution of lift-to-drag ratio of the different designs. The previous parametrization, based on the work of Van Luijk [17] had an L/D of 20.3 and serves as benchmark. The L/D ratio varies from design to design, reaching a maximum of 24.2 at design 8.

Figure 13 shows the lift distributions of the most efficient designs of every phase. The surplus of lift at the root of the baseline design and the lack of lift in the middle section are clear in the spanwise lift distribution. The subsequent phases show a more elliptical lift distribution. The section lift coefficient shows a decrease in section lift coefficient for all design phases near the root. Varying increases in section lift coefficient are seen in the middle section of the wing.

Downloaded by Technische Universiteit Delft on January 5, 2024 | http://arc.aiaa.org | DOI: 10.2514/6.2024-2669

Downloaded by Technische Universiteit Delft on January 5, 2024 | http://arc.aiaa.org | DOI: 10.2514/6.2024-2669

Table 4 Flying V iterations summarized

Iteration	L/D (-)	Description
Baseline	21.3	The baseline design is based on previous Flying V work, with the new parametrization.
Phase 1		
Design 1	22.9	The original NACA supercritical airfoils of the outboard wing had suboptimal performance. Based on the work of Faggiano[37] the airfoils of the outboard wing are changed. Also, the transition section profile is improved upon.
Design 2	23.1	Based on the results of Design 1, the lift at the root is lowered, the camber and aft-loading of the middle wing increased, profiles smoothened and incidence angles of the outboard wing are increased.
Design 3	22.5	This iteration tries to create an elliptical lift distribution based on the incidence angle and camber of different sections. Outboard profiles start to exceed their design lift coefficient.
Phase 2		
Design 4	22.1	Design 4 redistributes wing area from the inboard to the outboard wing, with the goal of reducing wetted area inboard and reducing lift coefficients outboard. The root chord is reduced by 25 cm, the tip chord increased by 15 cm. A decrease in efficiency is perceived.
Design 5	21.9	With the goal of wetted area reduction, the root chord is reduced by 25 cm in Design 5. The outboard wing is unaltered. A decrease in efficiency is perceived.
Design 6	23.9	Design 6 aims to reduce wetted area by reducing the chord length over the whole wing, but with smaller magnitudes than Design 4 and 5 (2.5cm). Increases in efficiency were perceived.
Phase 3		
Design 7	22.9	To reduce Mach number magnitudes on the outboard wing, a 2D optimization of the airfoils is performed and the airfoils are implemented on the Flying V. The 2D and 3D data did not correlate well.
Design 8	24.2	Design 8 incorporates airfoils found in Obert [43] on the outboard wing. This significantly reduced the Mach number magnitudes on the outboard wing and decreased shock losses at the wing-winglet junction.

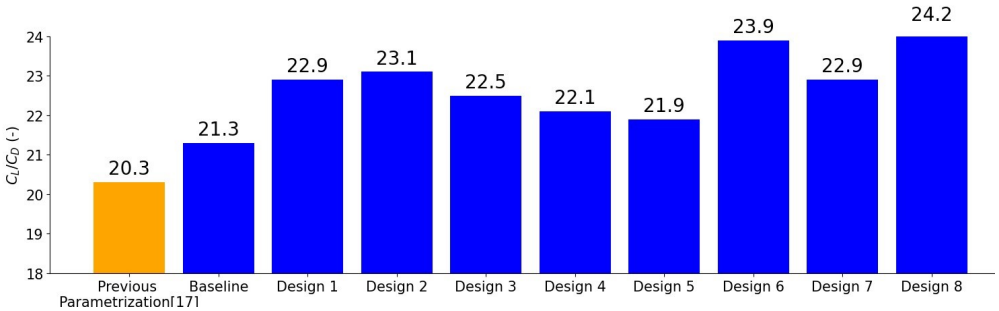

Fig. 12 Lift-to-drag ratios of different iterations performed

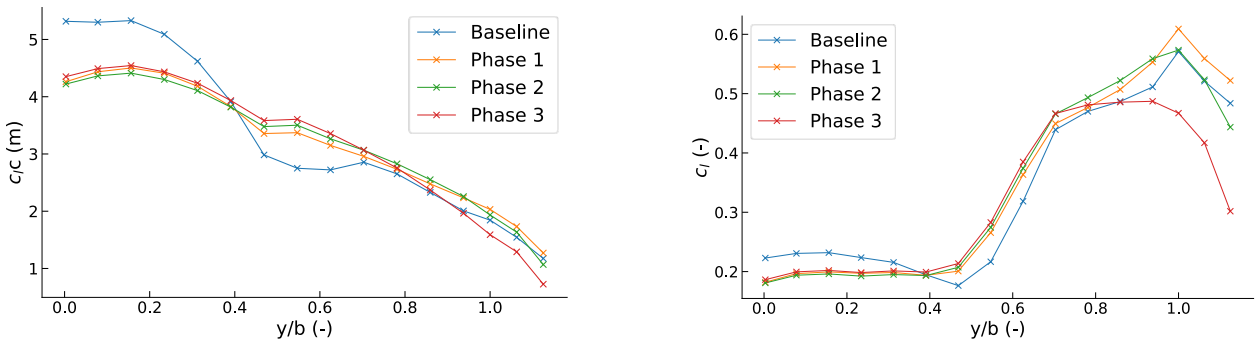

(a) Spanwise lift distributions **(b) Section lift distributions**

Fig. 13 Spanwise lift and section lift distributions of the different iteration phases (Mach =0.85, Re = 88.3 million, C_L = 0.26)

The final design (phase 3) shows a plateau of section lift coefficient at the outboard wing with a decrease of section lift coefficient at the winglet. The decrease in winglet loading is visualized in figure 15.

Figure 14 shows the Mach number isosurfaces on the wing. The relatively large supersonic area on the outboard wing of the baseline design leads to a relatively high wave drag, decreasing cruise performance. A clear root effect is visible, as the Mach isobars curve towards the root. This leads to shock formation near the trailing edge. Another important point is the large thickening of the boundary layer at the sections with the highest thickness-to-chord ratio (0.4<y/b<0.6). This effectively decambers the upper part of the section, decreasing lift near the trailing edge. The pressure distribution plots show this effect as upper and lower C_p curves tend to merge. Interference effects are recognizable at the wing-winglet junction. Between the Baseline and Design 6, the supersonic region on the outboard wing is reduced by optimization of twist and introduction of Faggiano's [14] airfoils. A higher magnitude of Mach numbers can be seen in the transition section. Design 8 shows significant improvements at the outboard wing.
Improvements can also be perceived at the wing-winglet junction (figure 15). The double shock pattern on the winglet is replaced by a single, weaker shock. The Mach numbers are reduced. Implementation of airfoils from Obert [43], as well as an optimization of the twist distribution are the main factors enabling these improvements

B. Flying V Root Tail

A strong root effect, concentrating the pressure isobars near the trailing edge, is present on the Flying V. The large sweep angle is the main cause of this root effect. Inspired by the YB-35/49 [‡] (figure 16a), a tail section at the trailing edge of the root could realign the isobars and reduce the shock strength. Furthermore, the added volume can be useful, for example for the auxiliary power unit.
Figure 16b shows a similar tail implemented on the Flying V. The tail trailing edge is positioned slightly higher than the original trailing edge. This, combined with the larger airfoil length, locally decreases the camber. This can be seen in the shock strength. In figure 17a the Mach isobars are spaced further apart. In figure 17b, the pressure distribution shows a smaller suction peak near the trailing edge for the tail configuration. This also reduces the strength of the shock. This tail configuration decreased the drag coefficient with 0.4 drag counts. With the increase in weight due to the structure the overall efficiency gains will be small, but the extended volume can be a useful addition and the reduced suction peak could mitigate operating limit root issues. A more detailed study of the tail geometry is required to see the impact of the tail on the structure and to optimize the design aerodynamically further.

C. Aerodynamic Characteristics of the Final Design

Design 8 showed the highest L/D with acceptable flight characteristics. This section gives an overview of the aerodynamic characteristics of this design. The final L/D achieved is 24.2

[‡]https://en.wikipedia.org/wiki/Northrop YB-49

Downloaded by Technische Universiteit Delft on January 5, 2024 | http://arc.aiaa.org | DOI: 10.2514/6.2024-2669

Downloaded by Technische Universiteit Delft on January 5, 2024 | http://arc.aiaa.org | DOI: 10.2514/6.2024-2669

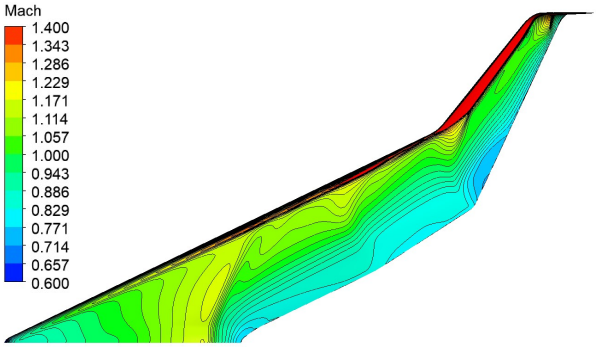

(a) Baseline

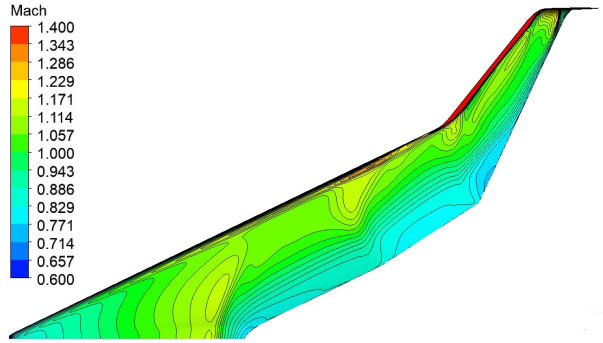

(b) Phase 1: Design 2

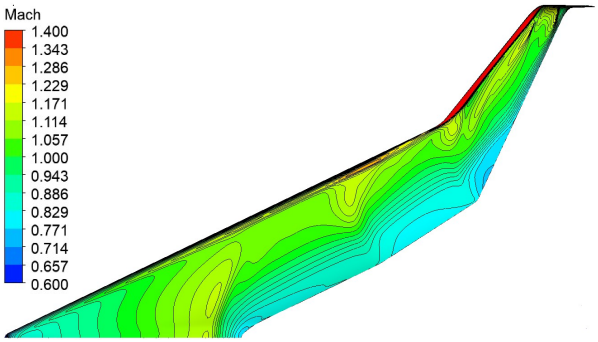

(c) Phase 2: Design 6

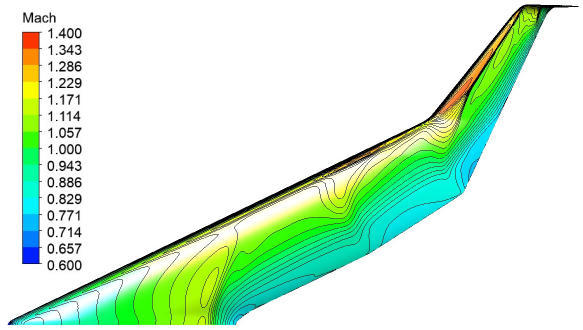

(d) Phase 3: Design 8

Fig. 14 Mach contours of different Flying V iterations (Mach =0.85, Re = 88.3 million, C_L = 0.26)

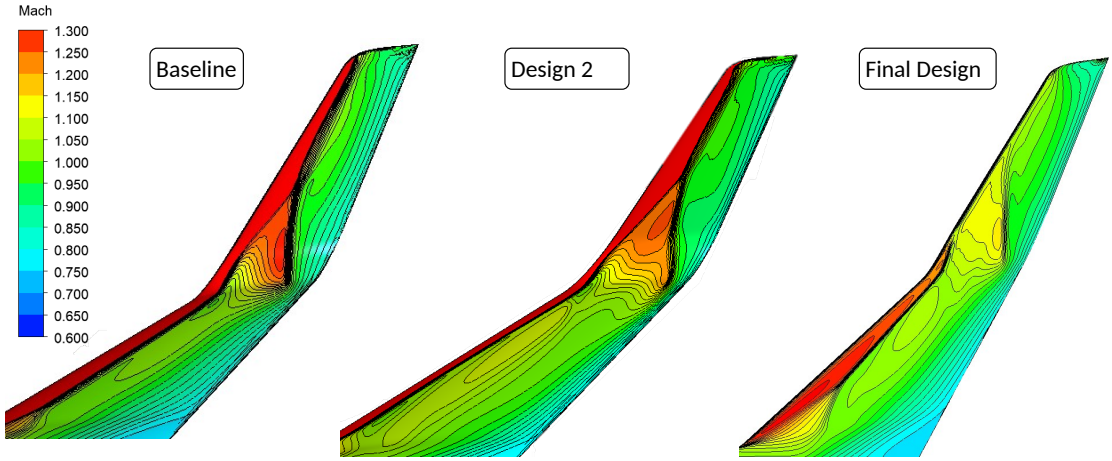

Fig. 15 Mach number contour of the wing-winglet interaction

Downloaded by Technische Universiteit Delft on January 5, 2024 | http://arc.aiaa.org | DOI: 10.2514/6.2024-2669

(a) YB-49 bomber prototype[1]

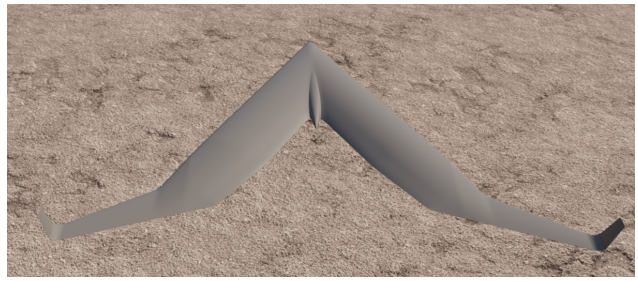

(b) Flying V, tail configuration

Fig. 16 YB-49 and Flying V showcasing a tail at the root

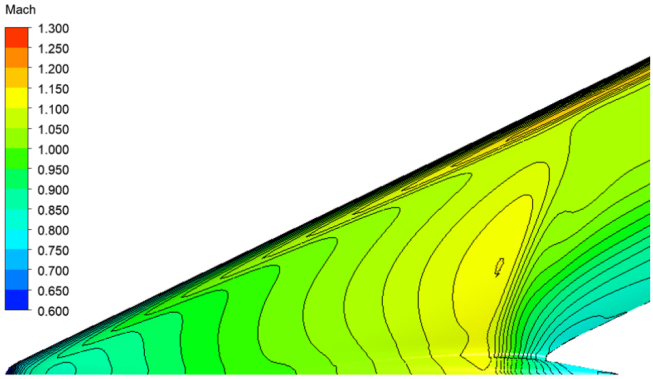

(a) Flying V, tail configuration Mach contours

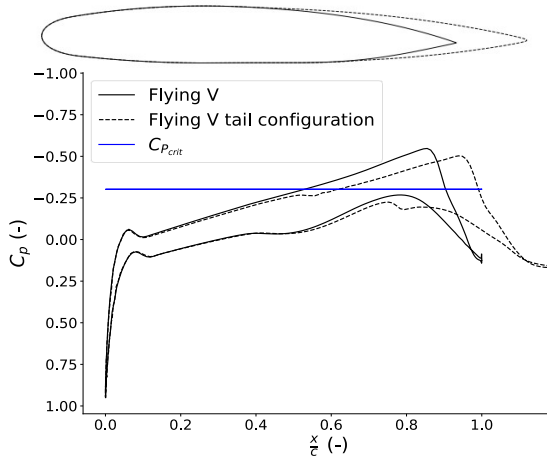

(b) Flying V, tail configuration root pressure distribution

Fig. 17 Flying V tail configuration(Mach =0.85, Re = 88.3 million, C_L = 0.26)

1. Cruise Characteristics

Figure 18 shows the camber, twist, thickness-to-chord ratio, lift and spanwise lift distributions of the final design. The maximum local camber is defined as the maximum distance between camber and chord line, divided by the chord length. An opposite trend in camber and twist angle is seen over the wingspan. As the camber is increased in the airfoil sections, the twist angle is decreased. A steep increase in camber can be perceived at the transition section. This results in an increase in local c_l. The thickness-to-chord ratio also starts to increase in the transition region. The blue line in the spanwise lift chart represents an elliptical lift distribution. Compared to previous iterations, the outboard wing is loaded relatively lower. The outboard wing shows a relatively triangular lift distribution. Even though a slightly less elliptical lift distribution is achieved, the reduced local lift coefficients help reduce wave drag and excessive magnitude of Mach numbers on the outboard wing. This is partly compensated by a higher lift at the root, where the flow conditions are less critical. The highest thickness-to-chord ratio is reached at approximately y/b = 0.45. A slight drop of lift is observed at this section.

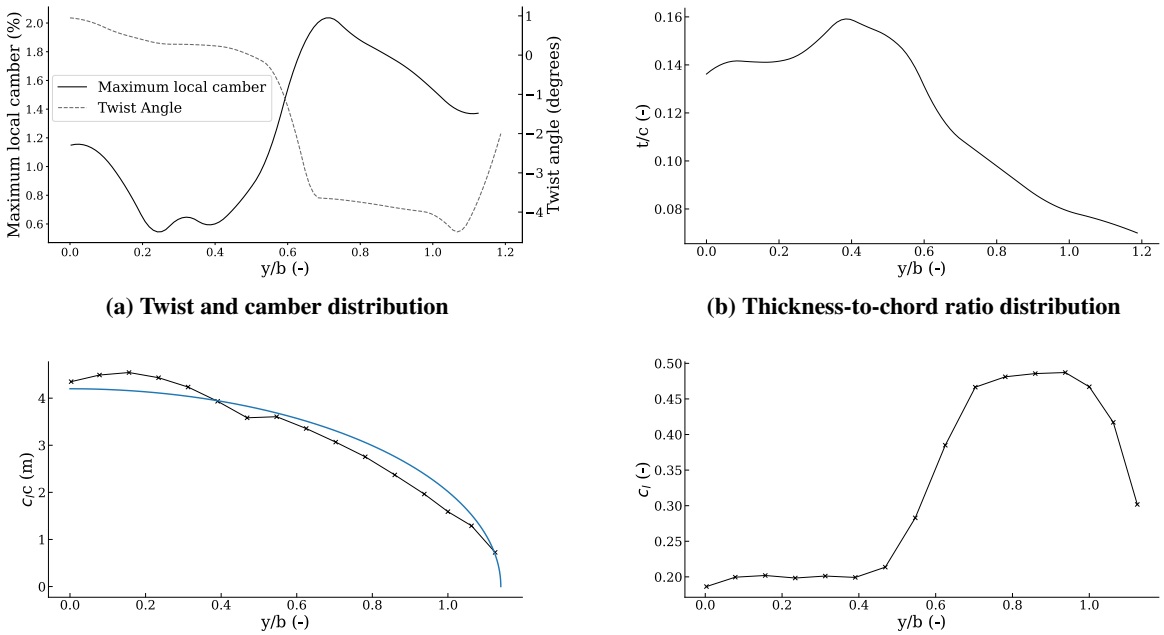

(a) Twist and camber distribution

(b) Thickness-to-chord ratio distribution

(c) Spanwise lift distribution

(d) Section lift distribution

Fig. 18 Wing twist, camber, t/c and lift distributions of the final design (Mach =0.85, Re = 88.3 million, C_L = 0.26)

Figure 19 shows the Mach number contour of the final wing. At the root reduced Mach numbers and a reduced shock strength are observed due to the lower loading and section optimization. The middle wing shows reduced suction peaks and an increase in aft-loading. A reduction in Mach numbers on the outboard wing is observed and double shocks on the winglet are mostly avoided. The highest Mach numbers at the leading edge kink are mostly isentropically recompressed.

A comparison of pressure distributions between the baseline and final design is shown in figure 20. At the root (figure 20a), the aforementioned root effect leads to a shock near the trailing edge. The middle sections of the wing (figure 20b) show a suction peak, followed by a region of relatively constant pressure/Mach numbers. Boundary layer thickening results in similar pressures on the upper and lower surfaces near the trailing edge. The thick, more highly loaded sections of the wing produce significantly more drag than the inner or outer parts of the wing. The relatively large area of lower pressure, which near the trailing edge has a component in the flight direction, causes significant pressure drag. The large t/c ratio increases the component of the pressure in the flight direction further. The final design does show improvements in this region compared to the baseline.

At the outboard wing, the maximum Mach number reached is reduced from 1.54 to 1.36. This high Mach number of the Baseline design was caused by interference effects at the wing-winglet junction. At the root of the outboard wing (figure 20c), the strong shock seen in the baseline is replaced by an area of isentropic recompression. In the middle

Downloaded by Technische Universiteit Delft on January 5, 2024 | http://arc.aiaa.org | DOI: 10.2514/6.2024-2669

Downloaded by Technische Universiteit Delft on January 5, 2024 | http://arc.aiaa.org | DOI: 10.2514/6.2024-2669

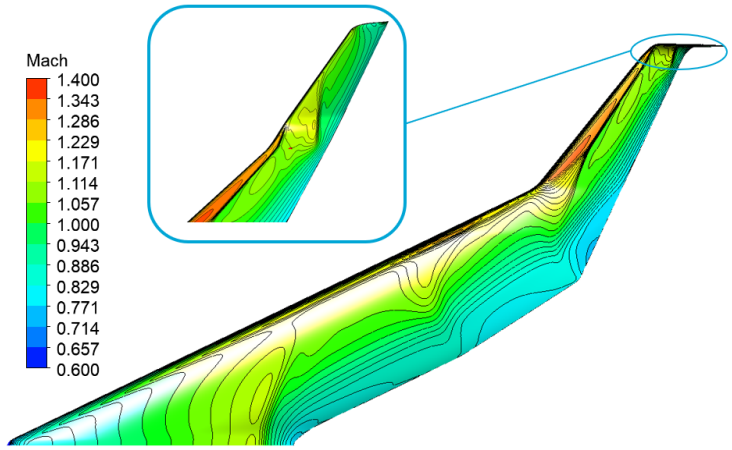

Fig. 19 Mach number contour of the final design (Mach =0.85, Re = 88.3 million, C_L = 0.26)

section of the outboard wing (figure 20d) a stronger shock is present. The shock strength is reduced compared to the Baseline design. A lack of front loading can be seen. The Mach number before the shock reaches 1.3, which is within the buffeting limits described by Obert [43]. At the wing-winglet junction (figure 20e) a significant decrease in shock strength of the first shock is seen. The second shock moves forward. Finally on the winglet near the root (figure 20f), the double shock is avoided. The thin airfoil leads to a pressure distribution with a large region of isentropic recompression and a weak shock. The redesigned outboard wing shows a significantly reduced magnitude of Mach numbers and should increase the performance near the high-speed aerodynamic limits.

The skin friction coefficient contour (figure 21) shows a large skin friction coefficient near the leading edge, which agrees with the thin boundary layer in this region. The skin friction coefficient quickly reduces after a shock due to the thickening of the boundary layer. The boundary layer thickening at the transition section of the wing, near the trailing edge kink, is also clearly visible. It is characterized by a low skin friction coefficient. Simulations at lower Reynolds numbers showed the occurrence of separation in this transition part of the wing. A critical section is the root, where the skin friction coefficient nears 0. Caused by the aft-shock, this remains an area of attention. The Flying V root tail configuration reduces this phenomenon.

2. Flight Performance and Off-Design Characteristics

Table 5 shows a summary of planform and aerodynamic characteristics of the ParaPy parametrization by Van Luijk [17] and the final design of this study. It should be noted that different methods used in both studies could lead to a slight discrepancy in values. The final design has a lower zero drag coefficient. A slightly higher Oswald efficiency factor is seen in the previous parametrization design. Even though the design by Van Luijk showed significant shock losses due to non-perfect transitions, the lift might be more elliptical. The Oswald efficiency factor was computed based on a quadratic lift polar, using least-squares regression to compute the slope $\frac{dC_d}{d(C_L^2)}$. It should be noted that the Oswald efficiency factor showed changing behaviour with different ranges of lift coefficients. The nonlinearities due to the transonic nature of the flow might cause discrepancies. The cruise angle of attack is increased in this study. The change in parameterization might have changed the local twist, requiring a higher cruise angle of attack.

Table 5 Comparison of aerodynamic and planform characteristics of the baseline and final design. Drag coefficients are in drag counts

	C_L	C_D	C_{Do}	AR	e	S_{ref}	$\frac{C_L}{C_D}_{\max}$	$C_{L_{\text{opt}}}$	AOA_{cruise}	$M_{\text{loc}_{\max}}$
Previous Parametrization [17]	0.26	128	72	4.82	0.867	876.5	20.7	0.31	1.2	1.41
Flying V Final Design	0.26	107	62	3.59	0.84	902	24.2	0.27	3.6	1.36

Downloaded by Technische Universiteit Delft on January 5, 2024 | http://arc.aiaa.org | DOI: 10.2514/6.2024-2669

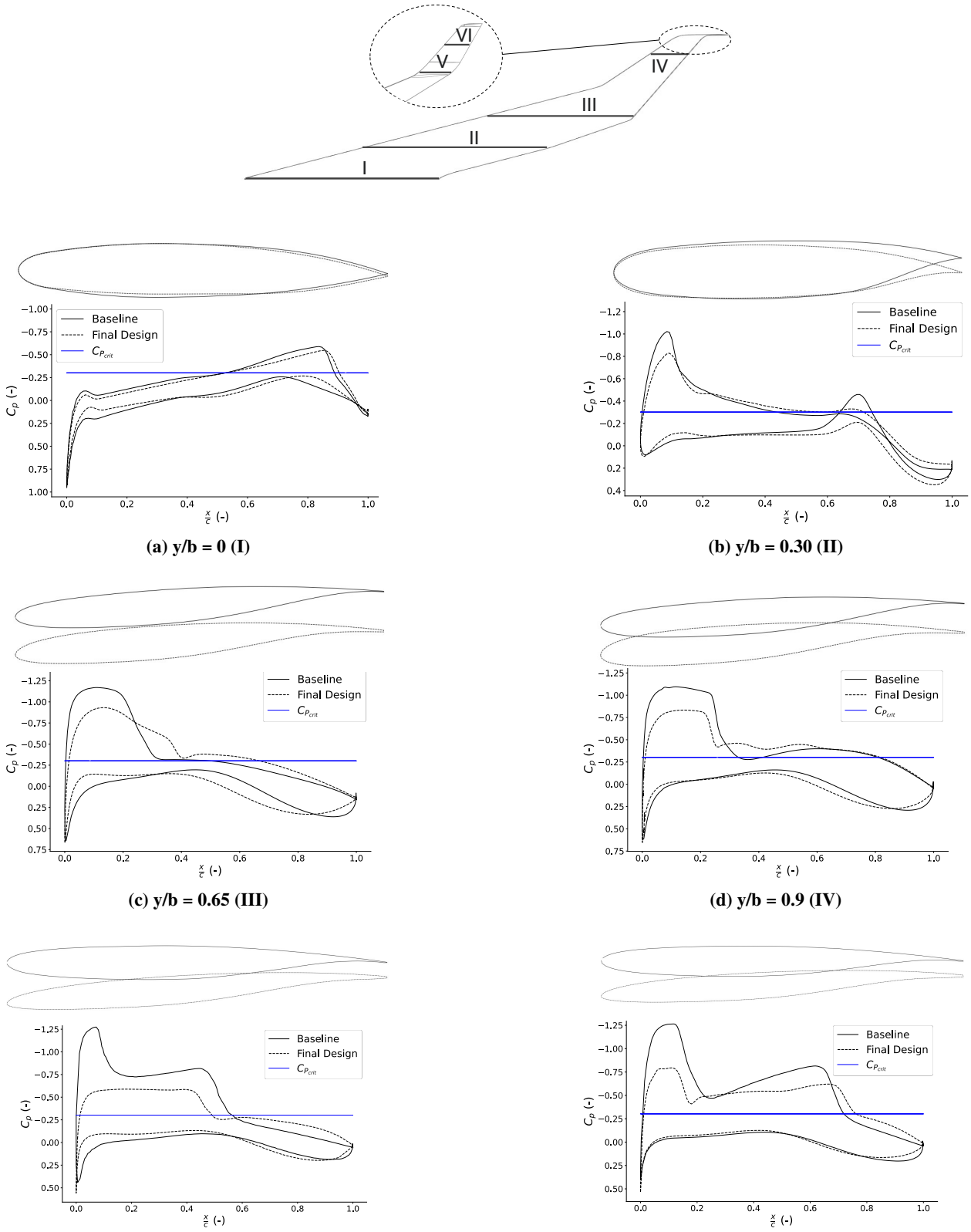

(a) y/b = 0 (I)

(b) y/b = 0.30 (II)

(c) y/b = 0.65 (III)

(d) y/b = 0.9 (IV)

(e) y/b = 1 (V)

(f) y/b = 1.06 (VI)

Fig. 20 Baseline (solid) and Final Design (dashed) sections and pressure distributions of the outboard wing (Mach =0.85, Re = 88.3 million, C_L = 0.26)

Downloaded by Technische Universiteit Delft on January 5, 2024 | http://arc.aiaa.org | DOI: 10.2514/6.2024-2669

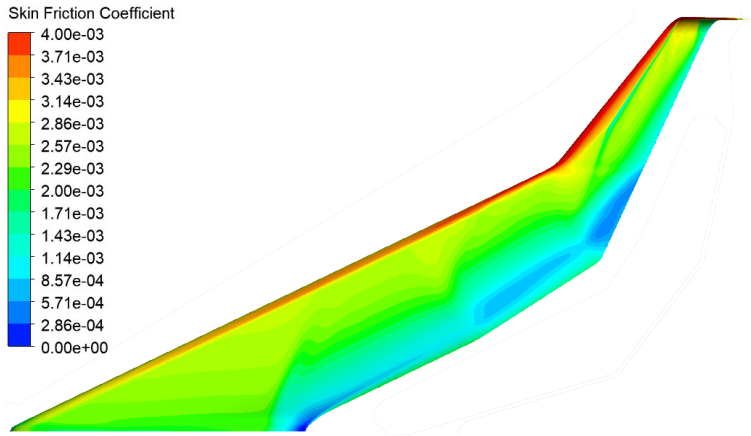

Fig. 21 Skin friction coefficient contour of the final design

Fig. 22 Flying V skin friction contour (Mach =0.85, Re = 88.3 million, C_L = 0.26)

Next to the aerodynamic efficiency, static longitudinal stability should be ensured, while minimizing trim drag. This requirement is quantified as equation 2. This ensures the neutral point is behind the center of pressure. The center of gravity can be designed such that it coincides with the center of pressure, ensuring static longitudinal stability and minimizing trim drag. Figure 23 shows the center of pressure and neutral point at different angles of attack in cruise conditions. The center of pressure moves backwards at increasing angle of attack, until non-linear behaviour starts occurring in the $C_L - \alpha$ curve. The center of pressure starts moving forward again at this point. This indicates the outboard wing starts stalling first. The wing has been designed such that the center of pressure, at the design lift coefficient of 0.26, is 2% of the mean aerodynamic chord length in front of the neutral point, which is a required static margin. The neutral point and center of pressure in design condition are located 32.7 and 32.4 meters from the nose of the aircraft respectively.

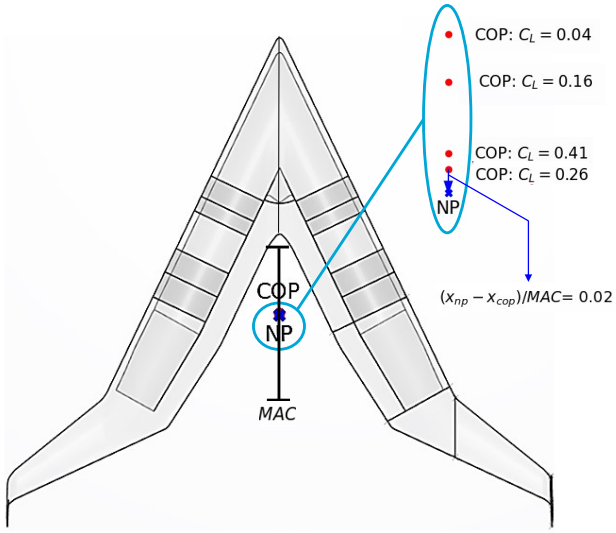

Fig. 23 Center of pressure (COP) and neutral point (NP) (Mach =0.85, Re = 88.3 million)

Figure 24 shows the off-design performance of the Flying V. The lift curve (figure 24a) shows linear behaviour up to an angle of attack of 5 degrees. It was already shown that the center of pressure starts to move forward around this angle of attack. The lift-to-drag ratio (figure 24b) also decreases rapidly in this angle of attack range. The maximum lift-to-drag ratio reached is 24.25 at an angle of attack of 3.79 with a C_L of 0.27. There is a plateau around the maximum L/D, so a wider range of lift coefficients remains efficient. The drag polar (figure 24c) shows parabolic behaviour, but wave

drag also plays a role in the drag polar. The drag divergence curve is presented in figure 24d. The drag divergence Mach number is taken as the Mach number where $\mathrm{d}C_D/\mathrm{d}M = 0.10$, used by Airbus and Douglas[44]. This occurs at a Mach number of 0.925. A plateau in drag coefficient is seen between Mach numbers of 0.75 and 0.85. Around the design Mach number the drag coefficient starts to rise as wave drag starts to increase. At a Mach number of 0.7, the drag coefficient rises slightly. This is caused by the increased angle of attack at lower Mach numbers, which leads to relatively high suction peaks and stronger shocks.

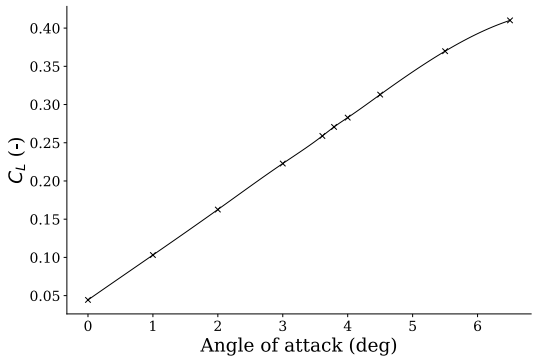

(a) Lift curve (Mach = 0.85, Re= 88.3e6)

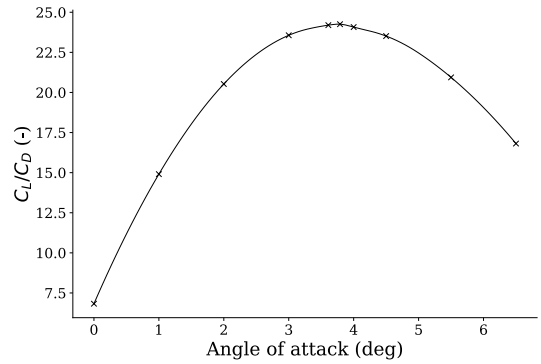

(b) Lift-to-drag ratio at different angles of attack (Mach = 0.85, Re= 88.3e6)

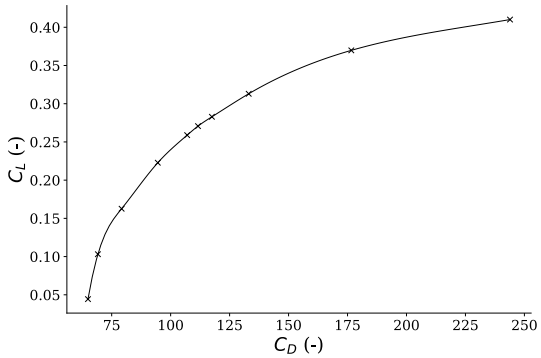

(c) Drag polar (Mach = 0.85, Re= 88.3e6)

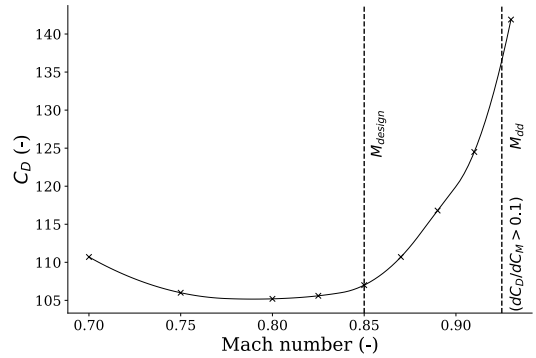

(d) Drag divergence curve ($C_L = 0.26$)

Fig. 24 Off-design curves at different flight conditions. The drag coefficient is reported in drag counts

Downloaded by Technische Universiteit Delft on January 5, 2024 | http://arc.aiaa.org | DOI: 10.2514/6.2024-2669

V. Conclusion

The objective of this research paper is to maximize the lift-to-drag ratio of the Flying V in cruise conditions by means of a high-fidelity CFD investigation. A third-order MUSCL Reynolds-averaged Navier-Stokes simulation with 15 million cells is validated using the ONERA M6 wing and shows excellent correlation to experimentally obtained pressure distributions at high subsonic conditions. A parameterized model with 97 design parameters is constructed that describes the outer mold line of the Flying V. Manual optimization steps are employed to incorporate various constraints and keep simulation costs within reasonable limits. The baseline design shows excessive wave drag on the outboard wing and a lack of spanwise lift at the mid-wing. Three manual design phases improve the aerodynamic performance while satisfying all constraints. Several iterations are conducted, during which the inner, mid and outboard wing sections are optimized, focusing both on elliptical lift and section performance. Improved airfoil sections in the outboard wing are shown to be better capable of efficiently generating the required lift coefficient for an elliptical lift distribution. Two-dimensional optimization of the outboard airfoil sections proved ineffective. The best design has a maximum lift-to-drag ratio of 24.2 at an angle of attack of 3.6 degrees in the design condition (Mach = 0.85, $C_L = 0.26$, Re = 88.3 million). The drag divergence Mach number is estimated at 0.925. While this study has shown the aerodynamic

efficiency of the Flying V design in cruise conditions, the whole flight envelope should be investigated to determine the overall feasibility of the design. The low skin friction coefficient at the root and transition section should be further investigated.

VI. Acknowledgements

We would like to thank Dr. Alexander Heidebrecht for his help with the early stages of the simulation set-up. His insights into structured meshing and simulation options were invaluable for the paper. Furthermore, the authors would like to thank the rest of the Flying V team for their help and insights during the research.

References

[1] Tuchhardt, R., and Hanson, K., "Special report on the impact of COVID-19 on air navigation service provision in Europe and the US," , Nov. 2021. URL https://transport.ec.europa.eu/news-events/news/special-report-impact-covid-19-air-navigation-service-provision-europe-and-us-2021-12-08_en.

[2] "Global Market Forecast | Airbus," , Jun. 2021. URL https://www.airbus.com/en/products-services/commercial-aircraft/market/global-market-forecast, section: Commercial Aircraft.

[3] NLR, "A ROUTE TO NET ZERO EUROPEAN AVIATION," , Feb. 2021. URL https://www.destination2050.eu/wp-content/uploads/2021/02/Destination2050_ExecutiveSummary.pdf.

[4] Kharina, A., and Rutherford, D., *Fuel Efficiency Trends for New Commercial Jet Aircraft: 1960 to 2014*, 2015.

[5] Schwader, R. L., "The Development of the Flying Wing," *Journal of Aviation/Aerospace Education & Research*, Vol. 8, No. 1, 1997. https://doi.org/10.58940/2329-258X.1212, URL https://commons.erau.edu/jaaer/vol8/iss1/4.

[6] Liebeck, R. H., "Design of the Blended Wing Body Subsonic Transport," *Journal of Aircraft*, Vol. 41, No. 1, 2004, pp. 10–25. https://doi.org/10.2514/1.9084, URL https://arc.aiaa.org/doi/10.2514/1.9084.

[7] Qin, N., Vavalle, A., Le Moigne, A., Laban, M., Hackett, K., and Weinerfelt, P., "Aerodynamic considerations of blended wing body aircraft," *Progress in Aerospace Sciences*, Vol. 40, No. 6, 2004, pp. 321–343. https://doi.org/10.1016/j.paerosci.2004.08.001, URL https://linkinghub.elsevier.com/retrieve/pii/S0376042104000569.

[8] Lyu, Z., and Martins, J. R. R. A., "Aerodynamic Design Optimization Studies of a Blended-Wing-Body Aircraft," *Journal of Aircraft*, Vol. 51, No. 5, 2014, pp. 1604–1617. https://doi.org/10.2514/1.C032491, URL https://arc.aiaa.org/doi/10.2514/1.C032491.

[9] Roman, D., Gilmore, R., and Wakayama, S., "Aerodynamics of High-Subsonic Blended-Wing-Body Configurations," *41st Aerospace Sciences Meeting and Exhibit*, American Institute of Aeronautics and Astronautics, Reno, Nevada, 2003. https://doi.org/10.2514/6.2003-554, URL https://arc.aiaa.org/doi/10.2514/6.2003-554.

[10] Meheut, M., Grenon, R., Carrier, G., Defos, M., and Duffau, M., "Aerodynamic Design of Transonic Flying Wing Configurations," 2009.

[11] Benad, J., "The Flying V A new Aircraft Configuration for Commercial Passenger Transport," 2015, p. 8 pages. https://doi.org/10.25967/370094, publisher: Deutsche Gesellschaft für Luft- und Raumfahrt - Lilienthal-Oberth e.V.

[12] Benad, J., *Luftfahrzeug*, Patent application DE102014201040A1, Airbus, 2014. URL https://register.dpma.de/DPMAregister/pat/PatSchrifteneinsicht?docId=DE102014201040A1.

[13] Benad, J., and Vos, R., "Design of a Flying V Subsonic Transport," *ICAS 2022*, 2022. URL https://repository.tudelft.nl/islandora/object/uuid%3A95ea413d-d5b1-4cb2-a650-828cb106dbbd.

[14] Faggiano, F., Vos, R., Baan, M., and Van Dijk, R., "Aerodynamic Design of a Flying V Aircraft," *17th AIAA Aviation Technology, Integration, and Operations Conference*, American Institute of Aeronautics and Astronautics, Denver, Colorado, 2017. https://doi.org/10.2514/6.2017-3589, URL https://arc.aiaa.org/doi/10.2514/6.2017-3589.

[15] Hillen, M., "Parametrisation of the Flying-V Outer Mould Line," 2020. URL https://repository.tudelft.nl/islandora/object/uuid%3Af4863ae4-2792-4335-b929-ff9dfdb6fed5.

Downloaded by Technische Universiteit Delft on January 5, 2024 | http://arc.aiaa.org | DOI: 10.2514/6.2024-2669

[16] Oosterom, W., and Vos, R., "Conceptual Design of a Flying-V Aircraft Family," *AIAA AVIATION 2022 Forum*, American Institute of Aeronautics and Astronautics, Chicago, IL & Virtual, 2022. https://doi.org/10.2514/6.2022-3200, URL https://arc.aiaa.org/doi/10.2514/6.2022-3200.

[17] Van Luijk, N., and Vos, R., "Constrained Aerodynamic Shape Optimisation of the Flying V Outer Wing," *AIAA AVIATION 2023 Forum*, American Institute of Aeronautics and Astronautics, San Diego, CA and Online, 2023. https://doi.org/10.2514/6.2023-3250, URL https://arc.aiaa.org/doi/10.2514/6.2023-3250.

[18] Benad, J., "Development of a numerical flow channel with the Lattice Boltzmann method and application to highly swept wings at high angles of attack," 2022. https://doi.org/10.14279/DEPOSITONCE-15208, URL https://depositonce.tu-berlin.de/handle/11303/16432, publisher: Technische Universität Berlin.

[19] Vos, R., Geuskens, F., and Hoogreef, M., "A New Structural Design Concept for Blended Wing Body Cabins," *53rd AIAA/ASME/ASCE/AHS/ASC Structures, Structural Dynamics and Materials Conference
20th AIAA/ASME/AHS Adaptive Structures Conference
14th AIAA*, American Institute of Aeronautics and Astronautics, Honolulu, Hawaii, 2012. https://doi.org/10.2514/6.2012-1998, URL http://arc.aiaa.org/doi/abs/10.2514/6.2012-1998.

[20] Benad, J., and Vos, R., *Aerial vehicle*, Patent application N2034242, Delft University of Technology, 2023.

[21] *Ansys Fluent Theory Guide*, ANSYS inc., 2022.

[22] Ferziger, J. H., and Perić, M., *Computational Methods for Fluid Dynamics*, Springer, Berlin, Heidelberg, 2002. https://doi.org/10.1007/978-3-642-56026-2, URL http://link.springer.com/10.1007/978-3-642-56026-2.

[23] Götten, F., Finger, D., Marino, M., Bil, C., Havermann, M., and Braun, C., "A review of guidelines and best practices for subsonic aerodynamic simulations using RANS CFD," 2019.

[24] *Ansys Icem CFD Help Manual*, ANSYS inc., 2021.

[25] Rumsey, C. L., and Wahls, R. A., "Focused Assessment of State-of-the-Art CFD Capabilities for Prediction of Subsonic Fixed Wing Aircraft Aerodynamics," 2008. URL https://ntrs.nasa.gov/citations/20080023857, nTRS Author Affiliations: NASA Langley Research Center NTRS Report/Patent Number: L-19484 NTRS Document ID: 20080023857 NTRS Research Center: Langley Research Center (LaRC).

[26] Tu, J., Yeoh, G. H., and Liu, C., *Computational fluid dynamics: a practical approach*, third edition ed., Butterworth-Heinemann, Amsterdam, 2018. URL https://www.sciencedirect.com/science/book/9780081011270.

[27] Roe, P. L., "Characteristic-Based Schemes for the Euler Equations," *Annual Review of Fluid Mechanics*, Vol. 18, No. 1, 1986, pp. 337–365. https://doi.org/10.1146/annurev.fl.18.010186.002005, URL https://www.annualreviews.org/doi/10.1146/annurev.fl.18.010186.002005.

[28] Pope, S. B., *Turbulent Flows*, 1st ed., Cambridge University Press, 2000. https://doi.org/10.1017/CBO9780511840531, URL https://www.cambridge.org/core/product/identifier/9780511840531/type/book.

[29] Hutchinson, B. R., and Raithby, G. D., "A MULTIGRID METHOD BASED ON THE ADDITIVE CORRECTION STRATEGY," *Numerical Heat Transfer*, Vol. 9, No. 5, 1986, pp. 511–537. https://doi.org/10.1080/10407788608913491, URL http://www.tandfonline.com/doi/abs/10.1080/10407788608913491.

[30] NPARC, "Verification Assessment," 2021. URL https://www.grc.nasa.gov/www/wind/valid/tutorial/verassess.html.

[31] Roache, P., Ghia, K., and White, "Procedure for Estimation and Reporting of Uncertainty Due to Discretization in CFD Applications," *Journal of Fluids Engineering*, Vol. 130, No. 7, 2008, p. 078001. https://doi.org/10.1115/1.2960953, URL http://FluidsEngineering.asmedigitalcollection.asme.org/article.aspx?articleid=1434171.

[32] Wilcox, D. C., *Turbulence Modeling for CFD*, 3rd ed., D C W Industries, La Cãnada, Calif, 2006.

[33] Blazek, J., *Computational Fluid Dynamics: Principles and Applications*, 3rd ed., Butterworth-Heinemann, Amsterdam, 2015.

[34] *ANSYS Fluent User's Guide*, ANSYS inc., 2013.

[35] Spalart, P., "Trends in turbulence treatments," *Fluids 2000 Conference and Exhibit*, American Institute of Aeronautics and Astronautics, Denver,CO,U.S.A., 2000. https://doi.org/10.2514/6.2000-2306, URL https://arc.aiaa.org/doi/10.2514/6.2000-2306.

Downloaded by Technische Universiteit Delft on January 5, 2024 | http://arc.aiaa.org | DOI: 10.2514/6.2024-2669

[36] Schmitt, V., and Charpin, F., "Pressure distributions on the ONERA M6 wing at transonic Mach numbers," 1979. URL https://www.semanticscholar.org/paper/Pressure-distributions-on-the-ONERA-M6-wing-at-Mach-Schmitt-Charpin/6498e2b6c38d7da95a07fe539bbf8525eba8f730.

[37] Faggiano, F., "Aerodynamic Design Optimization of a Flying V Aircraft," 2016. URL https://repository.tudelft.nl/islandora/object/uuid%3A0b1472a5-3aad-433c-9a64-242c84b114fd.

[38] Crovato, A., Almeida, H. S., Vio, G., Silva, G. H., Prado, A. P., Breviglieri, C., Guner, H., Cabral, P. H., Boman, R., Terrapon, V. E., and Dimitriadis, G., "Effect of Levels of Fidelity on Steady Aerodynamic and Static Aeroelastic Computations," *Aerospace*, Vol. 7, No. 4, 2020, p. 42. https://doi.org/10.3390/aerospace7040042, URL https://www.mdpi.com/2226-4310/7/4/42.

[39] Moigne, A. L., and Qin, N., "Variable-Fidelity Aerodynamic Optimization for Turbulent Flows Using a Discrete Adjoint Formulation," *AIAA Journal*, Vol. 42, No. 7, 2004, pp. 1281–1292. https://doi.org/10.2514/1.2109, URL https://arc.aiaa.org/doi/10.2514/1.2109.

[40] Araya, G., "Turbulence Model Assessment in Compressible Flows around Complex Geometries with Unstructured Grids," *Fluids*, Vol. 4, No. 2, 2019, p. 81. https://doi.org/10.3390/fluids4020081, URL https://www.mdpi.com/2311-5521/4/2/81.

[41] Nielsen, E. J., and Anderson, W. K., "Recent Improvements in Aerodynamic Design Optimization on Unstructured Meshes," *AIAA Journal*, Vol. 40, No. 6, 2002, pp. 1155–1163. https://doi.org/10.2514/2.1765, URL https://arc.aiaa.org/doi/10.2514/2.1765.

[42] Laar, Y., "Aerodynamic Design of a Flying V Aircraft in Transonic Conditions," 2023. URL https://repository.tudelft.nl/islandora/object/uuid%3A591093b2-5cdc-41c5-b564-3786f43d51db.

[43] Obert, E., *Aerodynamic Design of Transport Aircraft*, IOS Press, 2009. Google-Books-ID: V1DuJfPov48C.

[44] Vos, R., and Farokhi, S., *Introduction to Transonic Aerodynamics*, Fluid Mechanics and Its Applications, Vol. 110, Springer Netherlands, Dordrecht, 2015. https://doi.org/10.1007/978-94-017-9747-4, URL http://link.springer.com/10.1007/978-94-017-9747-4.

Downloaded by Technische Universiteit Delft on January 5, 2024 | http://arc.aiaa.org | DOI: 10.2514/6.2024-2669